Aerodynamic roughness of ice surfaces derived from high resolution topographic data

Aerodynamic roughness of ice surfaces derived from high resolution topographic data

Mark W. Smith[1], Duncan J. Quincey[1], Timothy Dixon[2], Robert G. Bingham[3], Jonathan L. Carrivick[1], Tristram D. L. Irvine-Fynn[4], and David M. Rippin[5]

[1] School of Geography and water@leeds, University of Leeds, Leeds, UK, LS2 9JT

[2] School of Earth and Environment, University of Leeds, Leeds, UK, LS2 9JT

[3] School of GeoSciences, University of Edinburgh, Drummond Street, Edinburgh, UK, EH8 9XP

[4] Centre for Glaciology, Department for Geography and Earth Sciences, Aberystwyth University, Aberystwyth, UK, SY23 3DB

[5] Environment Department, University of York, Heslington, York, UK, YO10 5DD

Corresponding author: M. W. Smith, School of Geography and water@leeds, University of Leeds, Leeds, UK, LS2 9JT. (m.w.smith@leeds.ac.uk)

Key Points

- High resolution topographic data permit better glacier ice aerodynamic roughness (z_0) estimates
- Spatial z_0 variability over three orders of magnitude with different temporal trajectories
- Glacier topographic roughness used to upscale z_0 measurements for distributed ablation modeling

Abstract

The aerodynamic roughness of glacier surfaces is an important component of energy balance models and meltwater runoff estimates through its influence on turbulent fluxes of latent and sensible heat. In a warming climate these fluxes are predicted to become more significant in

contributing to overall melt volumes. Ice aerodynamic roughness (z_0) is commonly estimated from measurements of ice surface microtopography, typically from topographic profiles taken perpendicular to the prevailing wind direction. Recent advances in surveying permit rapid acquisition of high resolution topographic data allowing revision of assumptions underlying conventional topographic profile-based z_0 measurement. This paper presents alternative methods of estimating z_0 directly from Digital Elevation Models (DEMs) or three-dimensional point clouds, and examines the spatial and temporal variability of z_0 across the ablation zone of a small Arctic glacier. Using Structure-from-Motion (SfM) photogrammetry to survey ice surfaces with millimeter-scale accuracy, z_0 variation over three orders of magnitude was observed but was unrelated to large scale topographic variables such as elevation or slope. Different surface-types demonstrated different temporal trajectories in z_0 through three days of intense melt, though the observed temporal z_0 variability was lower than the spatial variability. A glacier-scale topographic model was obtained through Terrestrial Laser Scanning (TLS) and sub-grid roughness was significantly related to z_0 calculated from a 2 m resolution DEM. Thus, glacier scale TLS or SfM surveys can characterize z_0 variability over a glacier surface and allow distributed representations of z_0 in surface energy balance models.

Index Terms

0738 Ice; 1814 Energy budgets; 1855 Remote sensing; 1863 Snow and ice; 1894 Instruments and techniques: modeling.

Keywords

aerodynamic roughness; ice surface energy balance; high resolution topography; anisotropy; Structure-from-Motion (SfM); Terrestrial Laser Scanning (TLS)

1. Introduction

In glacier surface energy balance models turbulent fluxes of sensible and latent heat are generally considered to be secondary to radiative heat fluxes [*Hock*, 2005]. However, they become increasingly influential (up to 80%) in overcast and windy conditions [*Holmgren*, 1971; *Marcus et al.,* 1984; *Giesen et al.,* 2014] and for glacierised regions characterized by maritime climates [*Hay and Fitzharris*, 1988; *Ishikawa et al.*, 1992]. Critically, their relative contribution to overall ice surface mass loss is predicted to become more significant in a warming climate [*Braithwaite and Olesen*, 1990], making it imperative that the key influences on turbulent fluxes are better understood. One of the most important of these influences is the aerodynamic roughness height z_0, which is related to ice-surface topographic roughness, in a complex way; and whose improved characterisation on glacier ice surfaces forms the focus of this paper.

All ice-melt models which aim explicitly to incorporate turbulent fluxes, in some way incorporate a value, or range of values, for z_0. This is because, in the absence of direct eddy correlation measurements (which are difficult to obtain in the field; *Greuell and Genthon*, [2004]), aerodynamic roughness height underpins the derivation of exchange coefficients for potential temperature and specific humidity in the surface boundary layer, which in turn are often used to approximate turbulent fluxes using the bulk aerodynamic method [*Hock*, 2005; *Brock et al.,* 2010]. However, z_0 is difficult to measure directly; different approximations are used in different studies. For example, spatially distributed surface energy balance models assume a uniform and constant value of z_0 [*Arnold et al*., 2006] and z_0 is also used as an optimized parameter in the fitting of model output to observations of glacier melt [*Hock and Holmgren*, 2005].

Uncertainty in z_0 values presents a serious challenge in the calculation of ice ablation with an order of magnitude change in z_0 leading to a factor of two change in estimated turbulent fluxes [*Munro*, 1989; *Hock and Holmgren,* 1996; *Brock et al.,* 2010]. Yet field studies have highlighted the

79 variability of z_0 over ice surfaces in both space and time. *Brock et al.* [2006] summarize z_0 values
80 for ice in the published literature, from 0.007 mm for Antarctic blue ice [*Bintanja and van den*
81 *Broeke,* 1994, 1995] to 80 mm for very rough glacier ice [*Smeets et al.,* 1999]. While values over
82 smooth ice are ~ 0.1 mm, the majority of glacier ice z_0 values are in the range of 1–5 mm [*Brock et*
83 *al.,* 2006]. Ablation zones of glaciers can exhibit a large range of ice surface roughness features;
84 however, attempts to model variations in z_0 over single valley glaciers to inform upscaling have
85 proven unsuccessful [*Brock et al.*, 2006]. Considering temporal variability of z_0, the systematic
86 increases in z_0 through the ablation season observed on snow surfaces [*Arnold and Rees,* 2003;
87 *Brock et al.,* 2006] are less pronounced on glacier ice which exhibits greater temporal variability in
88 z_0 [*Müller and Keeler*, 1969; *Smeets et al.*, 1999; *Denby and Smeets,* 2000; *Greuell and Smeets,*
89 2001; *Brock et al.,* 2006; *Smeets and van den Broeke*, 2008]. Such temporal variability remains
90 poorly quantified or constrained.
91
92 The calculation of z_0 from ice surface topography has retained assumptions put in place under
93 conditions of limited topographic data and computational power. The aim of this paper is to
94 address this shortcoming through application of recent advances in high resolution surveying to
95 estimate z_0 from ice surface topography. Specifically, we aim to:
96 [1] describe novel parameterizations of surface roughness to represent z_0 that utilize greater
97 availability of high resolution survey data;
98 [2] examine the spatial variability of ice z_0 over the ablation zone of a small Arctic glacier;
99 [3] investigate the possibility of upscaling microtopographic z_0 measurements to the glacier
100 scale; and
101 [4] characterize the temporal variability of z_0 as ice melt takes place.
102
103 **2. Origin, meaning and measurement of z_0**
104

105 z_0 is defined herein as a length scale that characterizes the loss of wind momentum attributable to
106 surface roughness [*Chappell and Heritage,* 2007]; i.e. the height above the ground surface at which
107 the extrapolated horizontal wind velocity drops to zero. The term arises as a constant of integration
108 from the fitting of logarithmic profiles to velocity data as specified by boundary layer theory
109 [*Prandtl*, 1926; *Millikan*, 1938] and is estimated for both water and air flows over a wide range of
110 surface types [*Smith*, 2014]. Thus z_0 is technically a property of the flow rather than of the surface.
111 This often overlooked distinction is highlighted by wind-tunnel experiments observing an increase
112 of z_0 with free-stream velocity (or shear velocity) over the same gravel surface where faster
113 aerodynamically rough flows transfer more momentum to the near surface [*Dong et al.,* 2002]. In
114 practice, z_0 is at least weakly related to surface properties, and relationships between z_0 and
115 microtopography are exploited frequently to obtain z_0 values.
116
117 With z_0 defined as a property of the air flow, velocity-profile based measurement would seem
118 preferable; however, there are a number of inherent difficulties in adopting this approach. Detailed
119 wind velocity profile measurements over sufficient durations are not always available [e.g. *Brock et*
120 *al.*, 2006; *Rees and Arnold,* 2006]; data requirements are certainly too onerous for distributed
121 measurement of z_0 in this way. Moreover, z_0 values derived from least-squares model fit to velocity
122 measurements are sensitive to instrumental errors [*Sicart et al.,* 2014]. On glaciers, temperature
123 inversions and katabatic winds often result in a wind speed maximum several meters above the
124 surface [e.g. *Wallén,* 1948; *Denby and Greuell*, 2000; *Giesen et al.,* 2014; *Sicart et al.,* 2014] and
125 thus deviate from the theoretical profile. Wind velocity profiles need to be adjusted for surface-
126 layer stability and definition of the surface height above which velocity profiles are measured is not
127 straightforward, particularly over rough surfaces [*Sullivan and Greeley,* 1993; *Smeets et al.*, 1999;
128 *Sicart et al.,* 2014]. Displacement heights are often defined to adjust the velocity profiles; however,
129 there is some uncertainty as to the appropriate level of the zero-reference plane [*Munro,* 1989;
130 *Andreas*, 2002].

Estimations of z_0 from surface microtopography show good agreement with velocity profile derived z_0 values [*MacKinnon et al.,* 2004]. From wind tunnel experiments on sand surfaces, grain-size approaches have been developed [*Bagnold,* 1941] where z_0 is quantified as $1/30^{th}$ of a grain diameter. This classic approach is inappropriate for complex ice surfaces that are not composed of individual grains and exhibit multiple scales of topographic variability. An equation developed by *Lettau* [1969] is used more frequently in studies on ice surfaces, where z_0 is quantified as

$$z_0 = 0.5h^* \left(\frac{s}{S}\right) \quad (1)$$

where h^* represents the average vertical extent of microtopographic variations (i.e. effective obstacle height, m), s is the silhouette area facing upwind (i.e. the roughness frontal area, m^2) and S is the unit ground area occupied by each element (i.e. the 'lot' area, m^2). The drag coefficient is represented with 0.5; an 'average' drag coefficient. The Lettau equation was developed from experiments placing several hundred bushel baskets in a field upwind of an anemometer mast. With such isolated and well-defined roughness elements, specification of each term in (1) is relatively straightforward and results agreed with profile-based z_0 values to ± 25%. However, on ice surfaces, both velocity profiles and surface roughness are more difficult to measure. Good agreement between eddy covariance, wind velocity profile and microtopographic measurement techniques over ice is often reported (e.g. *Brock et al.,* [2006]), though differences are also apparent. For example, *van den Broeke* [1996] observed little agreement between the velocity profile and microtopographic methods, calculating a z_0 of 0.8 mm from wind velocity profiles and 120 mm using the Lettau equation (the latter of which was thought to be more realistic for the energy balance).

156 Alternatives to (1) do exist; for example, *Sellers* [1965] estimates z_0 from h^* alone, calibrating a
157 power-law relationship empirically. Meanwhile *Counehan* [1971] and *Fryrear* [1985] use the plan
158 area of roughness elements in place of the frontal area, and *Theurer* [1973] developed an equation
159 that uses both metrics. A common simplification of the Lettau equation for complex roughness
160 fields encountered on ice was developed by *Munro* [1989] [section 3.4] and applied to topographic
161 profiles perpendicular to the wind direction. However, sheltering effects from upwind are not taken
162 into account and the ability of single profiles to represent roughness accurately is questionable.
163 High resolution topographic data of glacier surfaces are increasingly available [e.g. *Nield et al.,*
164 2012]. From a Digital Elevation Model (DEM) the variability of z_0 for different profiles within the
165 DEM can be reported [*Irvine-Fynn et al.*, 2014]. Yet with advances in surveying techniques and
166 computational power, the advantages of the *Munro* [1989] method in terms of minimal data
167 requirements and computational efficiency have become less relevant. Indeed, three-dimensional
168 point clouds of ice surfaces are generally degraded substantially before z_0 can be estimated,
169 resulting in substantial loss of potentially useful data. It is this shortcoming that this study seeks to
170 address, through the analysis of multiple point clouds derived from Kårsaglaciären, a small glacier
171 in northern Sweden.
172
173 **3. Methods and Field Site**
174
175 3.1 Field Site
176
177 Kårsaglaciären (68.358739 N, 18.323593 E) is a small (~ 1 km^2) mountain glacier located in the
178 Vuoittasrita massif, part of the Abisko mountains, on the border between arctic Sweden and
179 Norway (Figure 1A). It presently terminates at ~ 900 m.asl into a small ice-marginal lake that is
180 developing as the ice margin retreats from a bedrock ridge. Since around 1912 the glacier has been
181 in a state of near constant retreat, but with some isolated areas of minor advance noted [*Karlén*,

182 1973; *Bodin*, 1993]. Since the early 1940s the glacier has been included in the Swedish national
183 mass balance programme [*Ahlmann and Tryselius*, 1926; *Wallén*, 1948, 1949, 1959; *Karlén*, 1973;
184 *Bodin*, 1993]. Climatic conditions at Kårsa are split between maritime (winter) and continental
185 (summer) and dominant winds are katabatic (ice-flow parallel). *Wallén* [1948, 1949] estimated that
186 turbulent fluxes were responsible for ~40% of ablation at Kårsa.
187
188 3.2 Field data collection
189
190 *3.2.1 Large-Scale DEMs*
191 The ablation zone of Kårsaglaciären was surveyed in July 2013 using a RIEGL VZ-1000 terrestrial
192 laser scanner (TLS). While the maximum range of the instrument is stated to be 1400 m [*RIEGL,*
193 2012], absorbance of the narrow Class 1 infrared laser beam over the wet ice surface reduced the
194 observed maximum range here to ~ 400 m on wet ice surfaces. The theoretical data acquisition rate
195 was 100,000 points per second, but again this was reduced with lower point recovery on ice
196 surfaces. The manufacturer stated precision and accuracy is 0.005 m and 0.008 m respectively
197 [*RIEGL,* 2012]. A nominal spatial resolution of 0.1 m at 450 m range was applied resulting in an
198 angular increment of 0.012°. At large ranges, the laser beam divergence (stated as 0.003 mm m^{-1}) is
199 typically the largest source of error [*Carrivick et al.,* 2015] with beam widths of 0.015 m at 500 m
200 range. The relative orientation of the surface would also have influenced the laser beam footprint
201 through determining the angle of incidence.
202
203 Four TLS surveys of Kårsaglaciären were undertaken between 22nd and 24th July 2013 from scan
204 positions surrounding the ~1 km^2 lower glacier (Figure 1B). There was little overlap between the
205 scans on the glacier ice itself and so gaps in coverage resulted from occlusions behind obstacles or
206 negligible returns from wet ice surfaces oblique to the TLS survey sites (Figure 1C). The first three
207 scan positions were repeated after an interval of three days (25th and 26th July) to yield a second

topographic model of the glacier. Accessibility and laser absorbance by snow precluded the acquisition of topographic data from the accumulation zone of the glacier. For survey control, a network of six tripod-mounted static targets was established surrounding the survey area utilising bedrock outcrops and sites locally proud of the surrounding terrain (Figure 1B). Using a minimum of four targets visible from each scan position, the TLS surveys were co-registered into a single local co-ordinate system. The standard deviations (or 3D error) of the co-registrations were between 4.5 mm and 13.8 mm. The two merged scans of the lower glacier contained 15×10^6 and 9×10^6 points.

The open-source topographic point cloud analysis toolkit (ToPCAT) [*Brasington et al.,* 2012] was used to unify point densities and create two glacier DEMs. A DEM resolution of 2 m was specified and cells containing fewer than 4 points were discarded (~20% of total cells). The mean cell elevation was applied to represent the glacier surface elevation and the detrended standard deviation of elevations was used to represent sub-grid roughness [*Vericat et al.,* 2014; *Smith and Vericat,* 2015]. The grids of the two DEMs were aligned to enable a DEM of Difference (DoD) to be calculated. The DoD represents changes on the glacier over a three day interval; however, the days over which this interval spans are not identical for each scan owing different days of occupation.

3.2.2. Plot-scale topography

To characterize finer scale topographic variability, 31 plots were surveyed using Structure-from-Motion Multi-View Stereo (SfM-MVS) photogrammetric techniques. The scale-dependence of z_0 calculation is an important consideration [*Arnold and Rees,* 2003; *Fassnacht et al.,* 2009]. *Rees and Arnold* [2006] observed two scale-free domains (<0.1 m and >~1 m), suggesting that the intermediate region is characterized by a definite scale. They suggest that topographic data of sampling interval of < 0.01 m and length of > 1 m with millimetric vertical accuracy is required to best represent z_0. Thus, plots were approximately 2 m x 2 m in size and 20 digital photographs of 6

234 Megapixels were taken of each plot with a Canon PowerShot G11 digital SLR camera. Images
235 surrounding each plot were taken from 2 m above ground resulting in angular changes of < 20°
236 between adjacent camera locations to facilitate identification of correct keypoint correspondence
237 [*Moreels and Perona,* 2007; *Bemis et al.,* 2014]. Oblique convergent images were captured to avoid
238 the doming effect observed when exclusively vertical images are used [*James and Robson,* 2014;
239 *Smith and Vericat,* 2015]. Plots were distributed on the glacier surface to incorporate the greatest
240 possible range of surface type and topographic variability and to ensure, as far as possible, good
241 spatial coverage of the lower glacier surface (Figure 1B). Glacier surface types were classified into
242 qualitative categories including smooth/superimposed ice, runnels, cryoconite, sun cups, blocky
243 crystalline ice, supraglacial channels, dirty ice, light/medium/dense scree, shallow/deep crevasses
244 and snow.
245
246 Groups of photographs pertaining to each plot were imported into Agisoft Photoscan Professional
247 1.1.6, and SfM algorithms implemented, to estimate simultaneously camera positions, camera
248 intrinsic parameters and scene geometry (see *James and Robson* [2012] for further details). Five
249 reflective disk targets (50 mm diameter) were fixed into the ice in the plot corners and plot centre
250 and directed to face the nearest TLS scan position. The targets were identified in additional TLS
251 surveys undertaken from each scan position that were focused on each plot. The 3D co-ordinates of
252 each target (referenced to the same local co-ordinate system as the TLS surveys) were imported,
253 and a linear similarity transformation performed to scale and georeference each SfM point cloud.
254 Average georeferencing errors were sub-cm (see Supplementary Information Table S1). Using these
255 coordinates the intrinsic camera parameters and scene geometry were refined and the bundle
256 adjustment re-run to optimize the image alignment by minimising the sum of the reprojection error
257 and the georeferencing error. Both original and optimized point clouds were calculated and MVS
258 image matching algorithms performed to produce final dense point clouds (Figure 1D). Average
259 point density of the final plot point clouds was >300,000 points m^{-2}. ToPCAT was applied to the

plot-scale SfM-MVS surveys for the generation of a DEM of 5 mm resolution. While TLS surveys of each plot were performed as part of the georeferencing, the absorbance of the near-infrared laser by ice and snow was such that relatively few TLS points were observed within each plot (typically 500 points m^{-2}) but this was sufficient to validate the SfM-MVS point clouds.

To analyze the temporal variability of ice surface roughness, of the 31 plots, 9 were revisited after 3 days. TLS targets were replaced and re-surveyed as described above. Additionally, 3 of these 9 plots were re-surveyed again a few hours afterwards.

To facilitate upscaling, the extent of each plot was mapped onto the glacier-scale DEM. Plot extents and DEM cells did not align perfectly owing to the variability of plot spacing, so the mean sub-grid roughness value of all cells containing at least part of each plot was calculate to compare plot-scale and glacier-scale models. The DEM surveyed on the same day as the plot was used in each case.

3.2.3. Meteorological data

Air temperature was monitored every 30 minutes throughout the field campaign at an automatic weather station (AWS) located ~500 m down-valley of the glacier terminus. The AWS comprised a Campbell Scientific CR200 data logger connected to an air pressure, air temperature, relative humidity, wind speed and wind direction sensors. This AWS has been in operation since 2007 and mean July temperatures have been 8.6°C, compared to -10.6°C in February.

3.3 Validation of SfM surveys

TLS data co-incident and contemporaneous with each SfM plot survey were used to validate both non-optimized and optimized SfM dense point clouds. Cloud-to-cloud comparisons were conducted in CloudCompare. The 3D distance between each TLS point and its nearest neighbour in the dense

SfM-MVS cloud was computed and split into X, Y and Z components. Where either the X or Y components were >0.02 m, the validation point was discarded. The mean and median Z distances were calculated alongside the standard deviation and RMSE of the errors for each plot. Beam divergence and laser footprint long axis were calculated (after *Schürch et al.,* [2011]) to estimate the error of the TLS validation data. While only negligible differences between RMSE values for optimized and non-optimized SfM-MVS point clouds were observed (typically ~ 1 mm), for each plot the point cloud with the lowest RMSE was used for analysis.

3.4 z_0 calculation

Each plot-scale point cloud was rotated to be aligned with the prevailing wind direction, observed to be predominantly down-glacier. Point clouds were cropped to ensure an approximately equal number of rows and columns. We undertook three different approaches, described in sequence below, to estimate z_0 from the microtopographic roughness data acquired. The first follows the method of *Munro* [1989] for the purposes of comparison with previous studies; the remaining two present new methods which utilize the greater volume of roughness information that can be gathered using raw and gridded TLS and SfM data sets. Differences between the three methods are summarized in Table 1.

3.4.1 Profile-based approach

To estimate z_0 following *Munro* [1989], we simplify the Lettau equation (1) by assuming that h^* can be represented by twice the standard deviation of elevations of the detrended profile ($2\sigma_d$, m), with the mean elevation set to zero (Figure 2A). Roughness elements are modeled by calculating the number of upcrossings above the mean elevation (f) in any profile of length X (m). The frontal silhouette area of roughness elements in the profile is then estimated as

$$s = \frac{2\sigma_d X}{2f}$$

312 (2)

313 and the ground area occupied by each roughness element (so-called 'lot' area), S (m^2), is
314 approximated as

315

316 $$S = \left(\frac{X}{f}\right)^2.$$

317 (3)

318 Thus the aerodynamic roughness length for a given profile becomes

319

320 $$z_0 = \frac{f(\sigma_d)^2}{X}.$$

321 (4)

322 As demonstrated in Figure 2A, (4) makes the assumption of uniformly distributed roughness
323 elements of equal height along the profile. Despite this, *Munro* [1989] found that it performed well
324 as an approximation of z_0 differing by only 12% from the true z_0 value. Using this method, z_0 was
325 calculated for every profile ($n \approx 400$) in both orthogonal directions for each plot. Following
326 normality tests, the probability distribution of profile-based z_0 values was characterized by the mean
327 and standard deviation of values in each orthogonal direction.

328

329 *3.4.2. DEM-based approach*

330 Profile-based simplifications, while computationally efficient, discard large volumes of potentially
331 useful topographic data. Such simplifications are more appropriate for the situation faced by *Munro*
332 [1989] where, prior to the widespread application of TLS or SfM, limited manually measured point
333 data were available (~30 points) and more demanding z_0 calculation methods cannot be supported.
334 With a DEM-based approach, the following assumptions of the profile approach can be relaxed:

335 [1] All roughness elements are of equal height.

[2] All roughness elements are equally spaced.

[3] No sheltering of roughness elements occurs.

[4] The frontal area of roughness elements is equal for opposing wind directions (isotropy).

Considering the *Lettau* [1969] equation, a DEM-based approach enables the roughness frontal area s to be calculated directly (Figure 2B) for each cardinal wind direction, thereby relaxing assumptions [1], [2] and [4]. Sheltering (assumption [3]) is implicitly represented by including only frontal areas above the detrended zero plane. Calculating the combined roughness frontal area across the plot, the planar plot area is then used as the ground area S (since the 'lot' area per roughness element as specified by *Lettau* [1969] incorporates both the ground area of the roughness element and the surrounding plot area). Specifying the effective obstacle height h^* is more problematic. Considering assumption [3], only points that are above the detrended plane are considered and h^* is calculated as the mean deviation above this plane. Thus, four z_0 values are generated for each plot, one for each cardinal direction.

3.4.3. Point cloud-based approach

High resolution surveying techniques produce dense point clouds containing rich information that require summary even for DEM construction. Using several simplifying assumptions, the dense point clouds were employed here directly, for a further form of z_0 calculation as follows.

Raw point clouds are not of a uniform density as SfM-MVS may oversample more visible local topographic highs. To yield a uniformly distributed point cloud the plot point clouds were subsampled after detrending using an octree filter. Normal vectors for each point were computed using triangulation (Figure 2C) and normal vectors facing each cardinal direction were counted to represent s in each cardinal direction under the assumption that each represents a comparable surface area following octree subsampling. Points below the detrended plane and 'flat' surfaces

362 defined as having a normal vector greater than 80° from horizontal were not used in the estimation
363 of *s*. The plot area *S* was approximated by the total number of points in the cloud (approximating
364 the 3d surface area). Finally, the effective obstacle height was calculated as the mean height above
365 the detrended plane of all points above that plane.
366
367 **4. Results**
368
369 4.1 Validation of SfM-MVS
370
371 Quantitative comparison of SfM-MVS points with TLS survey points demonstrated good agreement
372 between the two datasets. Across all 27 plots for which validation data were available, the average
373 Mean Absolute Error (MAE) for non-optimized point cloudes was 8.47 mm. Optimized SfM-MVS
374 models performed slightly better (8.14 mm), though there was little observable difference between
375 them (full details in Tables S1 and S2). However, MAE values were an order of magnitude below
376 the mean of the estimated maximum error in the TLS points (69.66 mm) owing to the sometimes
377 long survey ranges and beam divergence. Restricting analysis to situations where modeled TLS
378 error was <10 mm, non-optimized and optimized MAE values were 6.02 and 5.55 mm respectively.
379 Given the much shorter survey range for SfM-MVS than TLS, it is reasonable to assume that
380 expected errors are lower from plot-scale SfM than for glacier-scale TLS and are mm-scale (see
381 *Smith and Vericat*, [2015]).
382
383 4.2 Spatial variability in ice z_0
384
385 *4.2.1. Comparison of z_0 calculations*
386

Table 2 shows the results for z_0 calculation from the three different methods. Using the concordance correlation [*Lin*, 1989, 2000] which measures agreement of variables rather than linearity, we found that when averaged in all directions the strongest agreement was between DEM-based and point-cloud-based z_0 calculations (ρ_c = 0.973), with lower agreement between profile-based z_0 values and both DEM-based (0.730) and cloud-based (0.620) values. Separating the values into orthogonal components showed weaker agreement but a similar pattern (Figure S1). In general, point-cloud-based z_0 values were the highest (and had the lowest inter-quartile range) and DEM-based values the lowest, though little difference was observed between the calculation methods (Table 2).

4.2.2. Variability of z_0 between plots

A wide range of z_0 values was observed across the 31 plots on the ablation zone of Kårsaglaciären (Figure 3A). Summary statistics are separated out by direction in Table 2 and values for each plot are provided in Table S3. All z_0 values were > 0.05 mm and the majority were < 3 mm. All plots containing deep crevasses and one containing shallow crevasses yielded values > 10 mm, comparable with those reported on very rough glacier ice [*Smeets et al.,* 1999]. Plots traversed by supraglacial channels exhibited consistently high z_0 values (>1 mm), while plots containing dirt cones on the ice surface also yielded locally high values. The presence of scree distributed over the ice surface also produces a high z_0 (~ 1 mm); however, the extent of debris cover is important with lower areal concentrations exhibiting a lower z_0 (particularly for the DEM-based approach). The lowest z_0 values were for surfaces classified as 'smooth', 'slushy' or 'superimposed' ice (< 0.3 mm). Intermediate values were observed for patches of snow cover, sun cups, runnels and patches classified as 'dirty ice' (with z_0 typically between 0.5 and 1 mm).

4.2.3. Variability of profile values within a plot

DEM and cloud-based methods generate a single value for the plot (for each cardinal direction), whereas extraction of profile-based z_0 values from a DEM enables multiple values to be compared for a single plot. Skewness-kurtosis tests confirmed normality of all sets of profiles; only one plot was not normal at $P < 0.01$ and all plots were normal at $P < 0.05$. With over 400 profile-based z_0 measurements in each direction per plot, analysis of the standard deviation of these values is informative (Figure 3B; Figure S2). Mean values are consistently in line with DEM-based and cloud-based values; however, the variability about that mean is substantial. For two plots, the standard deviation of z_0 is greater than the mean. In all cases the high standard deviation of >20% of the mean z_0 value presents an important sampling issue for conventional topographic profiles.

4.2.4. Anisotropy

In Table 2, the largest differences between z_0 calculation methods emerge when the directionality of surface roughness is considered. Following *Smith et al.* [2006], an anisotropy ratio (□) is calculated for comparison of surface roughness in wind parallel ($R_{\parallel}$) and wind-perpendicular ($R_{\perp}$) directions.

$$\Omega = \frac{R_{\parallel} - R_{\perp}}{R_{\parallel} + R_{\perp}} \quad (5)$$

This ratio tends towards 1 when $R_{\parallel}$ dominates, towards -1 when $R_{\perp}$ dominates, and 0 when roughness is isotropic. Setting the down-glacier direction as parallel to the prevailing wind, Figure 3C summarizes the variation of anisotropy values between z_0 calculations. Profile-based metrics indicate greater z_0 for glacier-flow parallel winds and exhibit the largest range, DEM-based metrics suggest generally isotropic surfaces and have the smallest range of values, whereas cloud-based

436 metrics highlight greater z_0 for winds blowing across the glacier. Detection of anisotropy thus
437 appears to be an important discriminant of the metrics examined here.
438
439 A breakdown by plot is provided in Table S3 and Figure S3. The most extreme anisotropy ratio
440 values (and the biggest differences between metrics) are observed in plots containing large surface
441 features, such as crevasses or supraglacial channels. The specific values are sensitive to the
442 orientation of the channel within the plot. However, no significant relationship was observed
443 between anisotropy and z_0. The presence of debris often resulted in positive anisotropy ratios.
444
445 While profile-based approaches only separate orthogonal components, DEM-based analyses
446 produced a z_0 value for each cardinal direction and point-cloud-based metrics can yield a z_0 value
447 for any given wind direction, though here, for comparability, only values for cardinal directions
448 have been calculated. The difference between z_0 for two opposing wind directions is summarized as
449 a percentage of the average z_0 value (for both directions). The DEM-based z_0 values exhibit greater
450 variability for opposing wind directions (32% and 22% for glacier flow parallel and perpendicular
451 components respectively) than cloud-based z_0 values (9% and 12% respectively).
452
453 4.3 Upscaling surface roughness to the glacier scale
454
455 Statistical relationships were explored between plot-scale z_0 and glacier-scale variables to provide a
456 basis for upscaling z_0 beyond the plot (Figure 4A-C). Large values of z_0 associated with crevasses
457 had a significant leverage over such statistical relationships. Thus, the four plots that comprise the
458 right-hand panel of Figure 3A were excluded from upscaling analysis. A further plot, located in the
459 accumulation area was excluded as there were insufficient co-incident TLS data.
460

461 No statistically significant relationships were observed between z_0 and plot mean elevation, plot
462 distance from glacier terminus or plot mean slope. However, a significant relationship was observed
463 between sub-grid TLS roughness and all three z_0 values; the relationship was strongest for DEM-
464 based z_0 values (Figure 4B). This relationship presented the possibility of upscaling z_0 estimates
465 beyond the plot to represent z_0 variability over the majority of the lower glacier (where data are
466 available). The relationship for DEM-based z_0 values was used to provide such a glacier scale z_0
467 map in Figure 4D using the first TLS survey as a basis for upscaling. As plot data were only reliable
468 where $z_0 < 3$ mm, only cells in this range were included.
469
470 After upscaling, areas of relatively high z_0 values were found to be associated with crevasse features
471 (Figure 4D) and the medial moraine running through the centre of the glacier. Considering only the
472 0.14 km^2 area of the ablation area of Kårsaglaciären for which sufficient TLS data were available to
473 estimate z_0, the mean modeled z_0 was 0.99 mm, the median value was 0.85 mm and the standard
474 deviation was 0.61 mm. This is likely to be an underestimate of z_0 as some notable areas of high
475 sub-grid roughness were not able to be included (e.g. close to the glacier terminus).
476
477 4.4 Temporal changes in z_0
478
479 *4.4.1 Glacier-scale changes*
480
481 Over the 3 day TLS survey interval, a substantial amount of ice surface lowering was observed
482 throughout the ablation zone (Figure 5A). To demonstrate that the observed lowering is not a survey
483 artefact, the change detected in two bedrock areas was compared with that seen on the ice surface
484 (Figure 5B and C). The two distributions are statistically different. Median change observed by TLS
485 over bedrock was 7.28 mm (over 7,532 m^2 outlined in bold in Figure 5A), whereas that observed on
486 ice surfaces was -206.99 mm (over 0.12 km^2). At higher elevations within the survey area, surface

lowering rates (~150 mm) are slightly less than at the glacier margins and across the lower parts of the glacier (~200 mm). Relatively high rates of lowering (~280 mm) were observed on the true right of the glacier which corresponds to the entry point of a stream running under the ice along the glacier margin, fed by a waterfall indicated in the lower left of Figure 5A. A large area at the true left margin of the glacier close to the south-facing bedrock outcrop also showed higher than average lowering (~250–300 mm). Large elevation changes (> 2 m) were also observed at the terminus where Kårsaglaciären calves into a small proglacial lake. Glacier advances and calving events can be clearly observed from the DoD at the terminus (Figure 5A) and represent the biggest elevation changes over the three day survey interval.

4.4.3. Plot-scale changes

The change in z_0 observed over the 9 resurveyed plots is summarized in Figure 6. Plots were resurveyed after an interval of 0.5, 3 and/or 3.5 days resulting in a maximum of four time periods for a single plot. Values for all three z_0 calculation metrics are presented, incorporating averaged values for all directions and values separated into both down-glacier and across-glacier averages. Analysis of the AWS record revealed that the period following 23rd July 2013 (Figure 5E) was considerably warmer than any time previously in the melt season of 2013 when average daily temperatures rarely rose above 10°C.

Despite high rates of surface lowering (e.g. Figure 5D), estimated z_0 values (Figure 6) remained relatively constant for three plots containing surface meltwater features (supraglacial channels or runnels). Decreases in z_0 were observed for plots where surface debris was observed (dirty ice or debris band) or which contained minor stress features (a shallow crevasse or crevasse traces), while increases in z_0 were observed where the ice was very smooth and on a plot pocked with cryoconite.

All three z_0 values were well correlated and, as reported in section 4.2.1, point-cloud-based z_0 values were typically highest while profile-based z_0 values had the highest variability.

Over three days, observed surface lowering was typically ~0.2 m; however, three plots exhibited much higher values >0.45 m. These rapidly lowering plots covered a wide range of z_0 values, including the more deeply incised of the two supraglacial channels and crevasse traces and smooth ice, all of which were located in the upper ablation zone towards the true left margin of the glacier. Overall, melt rates were positively correlated with degree days (r = 0.87, n = 24, P < 0.0001). The three rapidly lowering plots experienced melt rates between 10.2 and 11.1 mm K^{-1} day^{-1} while other plots were between 4.2 and 7.0 mm K^{-1} day^{-1}.

5. Discussion

5.1 Methods for calculating z_0 from topographic data

Previously, collection of topographic data suitable for z_0 calculation required either laborious and time-consuming measurement or the construction of bespoke equipment [e.g. *Herzfeld et al.*, 2000]. Recent advances in the acquisition of high resolution topography have revolutionized the study of Earth-surface processes [*Passalacqua et al.,* 2015], yet the calculation of z_0 from ice surface topography has typically retained assumptions put in place under conditions of limited topographic data and computational power. With these restrictions lifted, the DEM-based analysis presented herein permits frontal area exposed to a prevailing wind direction to be calculated explicitly over an ice (or snow) surface. Furthermore, with alternative approximations, z_0 can be rapidly estimated directly from point clouds.

More detailed comparison of calculation methods reveals three weaknesses in the conventional topographic profile-based approach. First, calculating z_0 from a single topographic profile presents a sampling issue given the variability of topographic profile-based values within a single plot (Figure 3B). Similar z_0 variability was also reported by *Irvine-Fynn et al*. [2014]. Second, while orthogonal profiles are often computed, the different frontal areas from two opposing wind directions cannot be resolved. DEM-based z_0 values for opposing wind directions differed by > 20% meaning conventional approaches may not be appropriate for anisotropic surfaces. Third, topographic profile-based z_0 values do not account for sheltering of an obstacle. With many ice-surface features streamlined either by wind or water flows having continuous topographic expressions for 10s of meters or more (sastrugi, for example; *Jackson and Carroll* [1978]), such an assumption is limiting for glacier surfaces. This important weakness is revealed when z_0 values are separated into orthogonal directions (Figure 3C).

In the extreme case where a crevasse or supraglacial channel is aligned perpendicular to the prevailing wind direction (Figure 7A) a detrended topographic profile will not detect this feature even if located within the crevasse or channel and would yield a relatively low z_0 value. Conversely, if the plot were rotated by 90° (Figure 7B) a detrended topographic profile perpendicular to the wind direction would yield a relatively high z_0 value. However, visual examination of the two plot surfaces in Figure 7 reveals that Plot A has a greater frontal area exposed to the prevailing wind, whereas Plot B is relatively streamlined to the wind direction. In this case computing z_0 using frontal area calculated from a DEM or approximated from a point cloud results in a higher z_0 for Plot A; the opposite of profile-based z_0 values. Such differences are not seen when uniform arrays of discrete roughness elements are present (from which the *Lettau* [1969] equation was derived) and are only significant where natural streamlined surfaces are the focus of study.

5.2 Spatial variability of z_0 and potential for upscaling

563

564 A wide range of z_0 values for ice surfaces is reported in the literature; yet in this study a similar
565 range of z_0 values was observed over a single glacier ablation area. Our mean z_0 value of ~ 1 mm
566 reflects the typical values reported in the literature [*Brock et al.,* 2006]. Indeed the 'typical' ice
567 roughness value of 0.66 mm that is applied in the glacier-scale distributed surface energy balance
568 model of *Arnold et al*. [2006] is similar to our median modeled value of 0.85 mm (Figure 4D).
569 However, considering DEM-based z_0 values in this study, variation over three orders of magnitude
570 was detected from 0.05 mm on superimposed ice to 22 mm for a deep crevasse. It is clear that a
571 single z_0 value cannot accurately represent the important contribution of z_0 to glacier melt.
572 Prominent surface features (e.g. crevasses) result in locally high z_0 values. Scale-dependency of z_0
573 values requires further investigation; however the sampling method used here captures the length
574 scales identified by *Rees and Arnold* [2006].

575

576 The significance of the relationship between z_0 calculated from plot-scale SfM-MVS and glacier-
577 scale TLS roughness suggests that the relevant components of topographic variability influencing z_0
578 can be approximated at the glacier scale. The modeled z_0 map presented in Figure 4D contains
579 substantial data gaps, though these could be filled with a dense network of survey stations.
580 Aggregation of heterogeneous z_0 values over areas representing an estimated fetch of the wind
581 permits comparison of wind-profile derived values [*Panofsky,* 1984]. With the increased ease of
582 data acquisition upscaling z_0 to represent the variability over the glacier-scale becomes a distinct
583 possibility. Existing large scale TLS [e.g. *Kerr et al.,* 2009; *Nield et al.,* 2012] and SfM-MVS [e.g.
584 *Immerzeel et al.,* 2014; *Ryan et al.,* 2015] survey campaigns demonstrate this enhanced capability
585 clearly.

586

587 5.3. Temporal variability of z_0

588

589 Our observations of temporal variability in ice surface roughness with surface melt were acquired
590 on Kårsaglaciären during a short period of relatively high air temperatures and agree with
591 previously reported findings [e.g. *Brock et al.,* 2000, 2006; *Smeets and van den Broeke*, 2008]. Ice
592 with surface debris or small amounts of dirt on the surface tended to become smoother, as did
593 surfaces exhibiting small crevasse features suggesting preferential melting out of protruding
594 roughness. Supraglacial channels did not exhibit such a decline in roughness possibly as down-
595 cutting kept pace with preferential melting.
596
597 Substantial surface melt was recorded over just 4 days (Figures 5 and 6). Average surface lowering
598 was 0.2 m and showed a similar association between surface melt rates and degree days as reported
599 for Norwegian glaciers by *Laumann and Reeh* [1993] (5.5-7.5 mm K^{-1} day^{-1}). Ablation rates are
600 similar to the maximum values reported in *Wallén* [1948]. Three plots showed substantially higher
601 melt rates; these could not be discriminated by surface roughness or other features and instead
602 appeared to reflect variation in incoming radiation being relatively flat plots positioned close to a
603 south-facing slope.
604
605 5.4. Further work
606
607 The alternative z_0 calculation methods introduced here require validation using velocity-profile or
608 eddy-correlation data [*Nield et al*., 2013]. Similarly, modeled z_0 variability at the glacier scale
609 requires validation both through finer scale measurements and through incorporation into spatially
610 distributed surface energy balance models that are in turn validated against proglacial stream
611 discharge measurements. With glacier-scale topography acquired through TLS or SfM-MVS, such
612 energy balance models have the potential to incorporate sophisticated models of insolation by
613 calculating shading from valley topography directly. Orthophotograph mosaics are a further output
614 of plot-scale SfM that could be used to estimate surface albedo directly [*Dumont et al.*, 2011;

615 *Rippin et al.*, 2015]. In addition, glacier-scale surveys may be able to bridge the gap between
616 microtopography and satellite remote sensing of glacier surfaces for a more extensive upscaling of
617 z_0 as demonstrated by *Blumberg and Greeley* [1993] and investigated on glacier surfaces by *Rees*
618 *and Arnold* [2006].
619
620 Calculation of z_0 from high resolution DEMs enables many long-standing assumptions to be
621 relaxed. However, further investigation as to the specific parameters used in z_0 calculation (detailed
622 in Table 1) is required. Sheltering of surfaces has been studied in detail in the atmospheric sciences
623 and in investigations of aeolian erosion [e.g. *Garratt,* 1992; *Bottema,* 1996; *Chappell and Heritage*,
624 2007]. While *Garratt* [1992] suggested a displacement height of $0.7h^*$ for most natural surfaces, the
625 assumption made in Table 1 (for DEM-based and cloud-based z_0 calculations) was that frontal areas
626 below the detrended plane level would be effectively sheltered. Certainly more sophisticated
627 sheltering parameterisations should be investigated [see *Chappell et al.*, 2010]. Similarly, the
628 average drag coefficient of 0.5 used here is likely to be an overestimate for many glacier surfaces
629 which tend to be streamlined [*Wieringa,* 1993; *Smeets et al.*, 1999] in at least one direction and
630 would thus exhibit a much lower drag coefficient [*Powell*, 2014]. As demonstrated in Figure 7, the
631 degree of streamlining and hence the drag coefficient may be dependent on the wind direction.
632
633 **6. Conclusions**
634
635 Through direct representation of the surface area of roughness elements more sophisticated
636 parameterisations of z_0 from ice surface topography can be realized from high-resolution three-
637 dimensional survey data. Properties of surface roughness that best represent the process of
638 momentum transfer from air flows to the ice surface can be quantified directly, enabling calculation
639 of z_0 from topographic data to better reflect the underlying theoretical equations. When averaged
640 over all cardinal wind directions, there is little difference between the novel DEM-based z_0 values

641 and values calculated from profiles using assumptions on the form of surface roughness. However,
642 large differences emerge when z_0 is calculated separately for each wind direction, particularly where
643 surface roughness is anisotropic.
644
645 The aerodynamic roughness of ice surfaces can be estimated at the glacier scale using a relationship
646 established between z_0 and sub-grid roughness of topographic models gridding at the meter-scale.
647 Such upscaling is important considering: (i) the wide variability of z_0 over three orders of magnitude
648 over a relatively small glacier ablation zone; (ii) the lack of a statistical relationship between z_0 and
649 more general topographic variables such as elevation and slope; and (iii) the relatively large effect
650 that z_0 variability has on estimations of turbulent heat fluxes and glacier ice melt, particularly in the
651 context of future climate warming. With increased availability of high resolution topographic data
652 at the glacier scale, surface energy balance models can incorporate distributed z_0 parameterisations
653 and better predict rates of ice loss under climate change scenarios.
654
655 **Acknowledgements**
656 Fieldwork was funded by EU INTERACT grants awarded to Bingham (LARGE) and Rippin
657 (SAGLA) and a grant from the Carnegie Trust for the Universities of Scotland awarded to
658 Bingham. We gratefully thank the Abisko Scientific Research Station (ANS) for hospitality and
659 logistical support and Kallax Flyg for helicopter support.
660
661 **References**
662
663 Ahlmann, H. W., and O. Tryselius (1929), Der Kårsa-Gletscher in Schwedisch-Lappland, *Geogr.*
664 *Ann.*, 11, 1–32.
665

666 Andreas, E. L. (2002), Parameterizing scalar transfer over snow and ice: a review, *J.*
667 *Hydrometeorology,* 3(4), 417–432.
668
669 Arnold, N. S., and W. G. Rees (2003), Self-similarity in glacier surface characteristics, *J. Glaciol.,*
670 49(167), 547–554.
671
672 Arnold, N. S., W. G. Rees, A. J. Hodson, and J. Kohler (2006), Topographic controls on the surface
673 energy balance of a high Arctic valley glacier, *J. Geophys. Res.,* 111, F02011,
674 doi:10.1029/2005JF000426.
675
676 Bagnold, R. A. (1941), *The Physics of Wind-blown Sand and Desert Dunes,* 265(10), Methuen,
677 London.
678
679 Bemis, S. P., S. Micklethwaite, D. Turner, M. R. James, S. Akciz, S. T. Thiele, and H. A. Bangash
680 (2014), Ground-based and UAV-Based photogrammetry: A multi-scale, high-resolution mapping
681 tool for structural geology and paleoseismology, *J. Structural Geology*, 69, 163−178.
682
683 Bintanja, R. and M. R. van den Broeke (1994), Local climate, circulation and surface-energy
684 balance of an Antarctic blue-ice area, *Ann. Glaciol.,* 20, 160–168.
685
686 Bintanja, R. and M. R. van den Broeke (1995), The surface energy balance of Antarctic snow and
687 blue ice, *J. Appl. Meteorol.,* 34(4), 902–926.
688
689 Blumberg, D. G., and R. Greeley (1993), Field studies of aerodynamic roughness length, *J. Arid*
690 *Environments*, 25 39–48.
691

692 Bodin, A. (1993), Physical properties of the Kårsa glacier, Swedish Lapland, Stockholm, University
693 of Stockholm, Department of Physical Geography, Research Report 17.
694
695 Bottema, M., (1996), Roughness parameters over regular rough surfaces: experimental requirements
696 and model validation. *J. Wind Eng. Ind. Aerodyn.*, 64, 249–265.
697
698 Braithwaite, R. J. and O. B. Olesen (1990), Response of the energy balance on the margin of the
699 Greenland ice sheet to temperature changes, *J. Glaciol.*, 36, 217–21.
700
701 Brasington, J., D. Vericat, and I. Rychkov (2012), Modelling river bed morphology, roughness and
702 surface sedimentology using high resolution terrestrial laser scanning, *Water Resour. Res.* 48,
703 W11519, doi:10.1029/2012WR012223.
704
705 Brock, B. W., I. C. Willis, M. J. Sharp, and N. S. Arnold (2000), Modelling seasonal and spatial
706 variations in the surface energy balance of Haut Glacier d'Arolla, Switzerland, *Ann. Glaciol.,* 31,
707 53–62.
708
709 Brock, B. W., I. C. Willis and M. J. Sharp (2006), Measurement and parameterization of
710 aerodynamic roughness length variations at Haut Glacier d'Arolla, Switzerland, *J. Glaciol.*, 52,
711 281–297.
712
713 Brock, B. W., C. Mihalcea, M. P. Kirkbride, G. Diolaiuti, M. E. J. Cutler, and C. Smiraglia (2010),
714 Meteorology and surface energy fluxes in the 2005–2007 ablation seasons at the Miage debris-
715 covered glacier, Mont Blanc Massif, Italian Alps, *J. Geophys. Res.,* 115, D09106,
716 doi:10.1029/2009JD013224.
717

718 Carrivick, J. L., M. W. Smith, and D. M. Carrivick (2015), High-resolution topography of the upper
719 Tarfala valley, *GFF*, 1−14.
720
721 Chappell, A., and G. L. Heritage (2007), Using illumination and shadow to model aerodynamic
722 resistance and flow separation: an isotropic study, *Atmospheric Environment*, 41, 5817−5830.
723
724 Chappell, A., S. Van Pelt, T. Zobeck, and Z. Dong (2010), Estimating aerodynamic resistance of
725 rough surfaces using angular reflectance, *Remote Sensing of Environment*, 114, 1462−1470.
726
727 Counehan, J. (1971), Wind tunnel determination of the roughness length as a function of the fetch
728 and the roughness density of three-dimensional roughness elements, *Atmospheric Environment*, 5,
729 637–642.
730
731 Denby, B., and W. Greuell (2000), The use of bulk and profile methods for determining surface
732 heat fluxes in the presence of glacier winds, *J. Glaciol.,* 46(154), 445–452.
733
734 Denby, B. and P. Smeets (2000), Derivation of turbulent flux profiles and roughness lengths from
735 katabatic flow dynamics, *J. Appl. Meteorol.,* 39(9), 1601–1612.
736
737 Dong, Z., X. Lui, and X. Wang (2002), Aerodynamic roughness of gravel surfaces,
738 *Geomorphology*, 43, 17−31.
739
740 Dumont, M., P. Sirguey, Y. Arnaud, and D. Six (2011), Monitoring spatial and temporal variations
741 of surface albedo on Saint Sorlin Glacier (French Alps) using terrestrial photography, *Cryosphere*,
742 5(3), 759−771.
743

744 Fassnacht, S. R., J. D. Stednick, J. S. Deems, and M. V. Corrao (2009), Metrics for assessing snow
745 surface roughness from digital imagery, *Water Resour. Res.,* 45, W00D31,
746 doi:10.1029/2008WR006986.
747
748 Fryrear, D. W. (1985), Soil cover and wind erosion, *Trans. ASAE*, 28, 781–784.
749
750 Garratt, J. R. (1992), *The Atmospheric Boundary Layer*, 336 pp., Cambridge atmospheric and space
751 science series, Cambridge University Press, Cambridge, U. K.
752
753 Giesen, R. H., L. M. Andreassen, J. Oerlemans, and M. R. Van Den Broeke (2014), Surface energy
754 balance in the ablation zone of Langfjordjøkelen, an arctic, maritime glacier in northern Norway, *J.*
755 *Glaciol.,* 60(219), 57–70.
756
757 Greuell, W., and C. Genthon (2004), Modelling land-ice surface mass balance. *Mass Balance of the*
758 *Cryosphere: Observations and Modelling of Contemporary and Future Changes*, 117–168.
759
760 Greuell, W., and P. Smeets (2001), Variations with elevation in the surface energy balance on the
761 Pasterze (Austria), *J. Geophys. Res.,* 106(D23), 31717–31727.
762
763 Hay, J. E., and B. B. Fitzharris (1988), The synoptic climatology of ablation on a New Zealand
764 glacier, *J. Climatology*, 8, 201–215.
765
766 Herzfeld, U. C., H. Mayer, W. Feller, and M. Mimler (2000), Geostatistical analysis of glacier-
767 roughness data, *Ann. Glaciol.*, 30, 235–242.
768

769 Hock, R. (2005), Glacier melt: a review of processes and their modelling, *Progress in Physical*
770 *Geography*, 29(3), 362-391.
771
772 Hock, R., and B. Holmgren (1996), Some aspects of energy balance and ablation of Storglaciären,
773 northern Sweden, *Geogr. Ann.,* 78A(2–3), 121–131.
774
775 Hock, R., and B. Holmgren (2005), A distributed surface energy-balance model for complex
776 topography and its application to Storglaciären, Sweden, *Journal of Glaciology*, 51(172), 25–36.
777
778 Holmgren, B. (1971), *Climate and energy exchange on a sub-polar ice cap in summer. Arctic*
779 *Institute of North America Devon Island Expedition 1961-1963,* Uppsala, Meteorologiska
780 Institutionen, Uppsala Universitet, Meddelande 107, Part A-E.
781
782 Immerzeel W. W., P. D. A. Kraaijenbrink, J. M. Shea, A. B. Shrestha, F. Pellicciotti, M. F. P.
783 Bierkens, and S. M. de Jong (2014), High-resolution monitoring of Himalayan glacier dynamics
784 using unmanned aerial vehicles, *Remote Sensing of Environment*, 150, 93–103.
785
786 Irvine-Fynn, T. D. L., E. Sanz-Ablanedo, N. Rutter, M. W. Smith, and J. H. Chandler (2014),
787 Measuring glacier surface roughness using plot-scale, close-range digital photogrammetry, *J.*
788 *Glaciol.*, 60, 957–969.
789
790 Ishikawa, N., I. F. Owens, and A. P. Sturman (1992), Heat balance characteristics during fine
791 periods on the lower parts of the Franz Josef Glacier, South Westland, New Zealand, *Int. J. of*
792 *Climatology*, 12(4), 397–410.
793

794 Jackson, B. S., and J. J. Carroll (1978), Aerodynamic roughness as a function of wind direction over
795 asymmetric surface elements, *Bound.-Lay. Meteorol.,* 14, 323–330.
796
797 James, M. R., and S. Robson (2012), Straightforward reconstruction of 3D surfaces and topography
798 with a camera: accuracy and geoscience application, *J. Geophys. Res.: Earth Surface* 117, F03017,
799 doi: 10.1029/2011JF002289.
800
801 James, M. R., and S. Robson (2014), Mitigating systematic error in topographic models derived
802 from UAV and ground-based image networks, *Earth Surf. Processes Landforms*, 39, 1413–1420,
803 doi: 10.1002/esp.3609.
804
805 Karlén, W. (1973), Holocene glacier and climatic variations, Kebnekaise Mountains, Swedish
806 Lapland, *Geogr. Ann.*, 55A(1), 29–63.
807
808 Kerr, T., I. Owens, W. Rack, and R. Gardner (2009), Using ground-based laser scanning to monitor
809 surface change on the Rolleston Glacier, New Zealand, *J. Hydrol.,* 48, 59–71.
810
811 Laumann, T., and N. Reeh (1993), Sensitivity to climate change of the mass balance of glaciers in
812 southern Norway, *J. Glaciol.*, *39*, 656–665.
813
814 Lettau, H. H. (1969), Note on aerodynamic roughness parameter estimation on the basis of
815 roughness element description, *J. Applied Meteorology*, 8, 828–832.
816
817 Lin, L. I.-K. (1989), A concordance correlation coefficient to evaluate reproducibility, *Biometrics*,
818 45, 255–268.
819

820 Lin, L. I. -K. (2000), A note on the concordance correlation coefficient, *Biometrics*, 56, 324–325.
821
822 MacKinnon, D. J., G. D. Clow, R. K. Tigges, R. L. Reynolds, and P. S. Chavez (2004), Comparison
823 of aerodynamically and model-derived roughness lengths (z_0) over diverse surfaces, central Mojave
824 Desert, California, USA, *Geomorphology*, 63(1), 103–113.
825
826 Marcus, M. G., R. D. Moore, and I. F. Owens (1984), Short-term estimates of surface energy
827 transfers and ablation on the lower Franz Josef Glacier, South Westland New Zealand, *New Zealand*
828 *J. Geology and Geophys.*, 28, 559–67.
829
830 Millikan, C. M. (1938), A critical discussion of turbulent flows in channels and circular tubes,
831 *Proceedings of the 5th International Congress on Applied Mechanics Cambridge, MA*, 386–392.
832
833 Moreels, P., and P. Perona (2007), Evaluation of features detectors and descriptors based on 3d
834 objects, *Int. J. Comp. Vis.*, 73(3), 263–284.
835
836 Müller, F., and C. M. Keeler (1969), Errors in short-term ablation measurements on melting ice
837 surfaces, *J. Glaciol.,* 8(52), 91–105.
838
839 Munro, D. S. (1989), Surface roughness and bulk heat transfer on a glacier: comparison with eddy
840 correlation, *J. Glaciol.,* 35(121), 343–348.
841
842 Nield, J. M., R. C. Chiverrell, S. E. Darby, J. Leyland, L. H. Vircavs, and B. Jacobs (2012),
843 Complex spatial feedbacks of tephra redistribution, ice melt and surface roughness modulate
844 ablation on tephra covered glaciers, *Earth Surf. Processes Landforms*, 38(1), 95–102.
845

Nield, J. M., J. King, G. F. Wiggs, J. Leyland, R. G. Bryant, R. C. Chiverrell, S. E. Darby, F. D. Eckardt, D. S. G. Thomas, L. H. Vircavs, and R. Washington (2013), Estimating aerodynamic roughness over complex surface terrain, *J. Geophys. Res.: Atmospheres*, *118*(23), 12–948.

Panofsky, H. A. (1984), Vertical variation of the roughness length at the boulder atmospheric observatory, *Bound.-Lay. Meteorol.,* 28, 305–308.

Passalacqua, P., P. Belmont, D. M. Staley, J. D. Simley, J. R. Arrowsmith, C. A. Bode, C. Crosby, S. B. DeLong, N. F. Glenn, S. A. Kelly, D. Lague, H. Sangireddy, K. Schaffrath, D. G. Tarboton, T. Wasklewicz, and J. M. Wheaton (2015), Analyzing high resolution topography for advancing the understanding of mass and energy transfer through landscapes: A review, *Earth-Science Reviews*, *148*, 174–193.

Powell, D. M. (2014), Flow resistance in gravel-bed rivers: Progress in research, *Earth-Science Reviews*, 136, 301–338.

Prandtl, L. (1926), Über die ausgebildete Turbulenz, *Proceedings of the 2nd International Congress of Applied Mechanics Zürich*, 62−74.

Rees, W. G. and N. S. Arnold (2006), Scale-dependent roughness of a glacier surface: implications for radar backscatter and aerodynamic roughness modelling, *J. Glaciol.*, 52, 214−222.

RIEGL (2012), Data Sheet Riegl VZ-1000. http://www.riegl.com/uploads/tx_pxpriegldownloads/DataSheet_VZ-1000_2015-03-24.pdf (Date Accessed 21st August 2015).

872 Rippin, D. M., A. Pomfret, and N. King (2015), High resolution mapping of supraglacial drainage
873 pathways reveals link between micro-channel drainage density, surface roughness and surface
874 reflectance, *Earth Surf. Processes Landforms*, doi: 10.1002/esp.3719.
875
876 Ryan J. C., A. L. Hubbard, J. E. Box, J. Todd, P. Christoffersen, J. R. Carr, T. O. Holt and N.
877 Snooke (2015), UAV photogrammetry and structure from motion to assess calving dynamics at
878 Store Glacier, a large outlet draining the Greenland ice sheet, *The Cryosphere*, 9(1), 1–11.
879
880 Schürch, P., A. L. Densmore, N. J. Rosser, M. Lim, and B. W. McArdell (2011) Detection of
881 surface change in complex topography using terrestrial laser scanning: application to the Illgraben
882 debris-flow channel, *Earth Surf. Processes Landforms* 36(14), 1847–1859.
883
884 Sellers, W. (1965), *Physical Climatology*, 272 pp., University of Chicago Press, Chicago.
885
886 Sicart, J. E.,M. Litt, W. Helgason, V. B. Tahar, and T. Chaperon (2014), A study of the atmospheric
887 surface layer and roughness lengths on the high-altitude tropical Zongo glacier, Bolivia, *J. Geophys.*
888 *Res. Atmos.,* 119, 3793–3808, doi:10.1002/2013JD020615.
889
890 Smeets, C. J. P. P., and M. R. van den Broeke (2008), Temporal and spatial variations of the
891 aerodynamic roughness length in the ablation zone of the Greenland ice sheet, *Bound.-Lay.*
892 *Meteorol.*, *128*(3), 315–338.
893
894 Smeets, C. J. P. P., P. G. Duynkerke and H. F. Vugts (1999), Observed wind profiles and turbulence
895 fluxes over an ice surface with changing surface roughness, *Bound.-Lay. Meteorol.,* 92(1), 101–123.
896

897 Smith, B. E., C. F. Raymond, and T. Scambos (2006), Anisotropic texture of ice sheets, *J. Geophys.*
898 *Res.*, 111, F01019, doi:10.1029/2005JF000393.
899
900 Smith, M. W. (2014), Roughness in the Earth Sciences, *Earth-Science Reviews*, 136, 202–225. doi:
901 10.1016/j.earscirev.2014.05.016.
902
903 Smith, M. W., and D. Vericat (2015), From experimental plots to experimental landscapes:
904 topography, erosion and deposition in sub-humid badlands from Structure-from-Motion. *Earth Surf.*
905 *Processes Landforms*, doi:10.1002/esp.3747.
906
907 Sullivan, R., and R. Greeley (1993), Comparison of aerodynamic roughness measured in a field
908 experiment and in a wind tunnel simulation, *Journal of Wind Engineering and Industrial*
909 *Aerodynamics*, 48(1), 25–50.
910
911 Theurer, W. (1973), Dispersion of ground-level emissions in complex built-up areas, Ph.D. Thesis,
912 University of Karlsruhe, Germany (in German).
913
914 van den Broeke, M. (1996), Characteristics of the lower ablation zone of the west Greenland ice
915 sheet for energy-balance modelling, *Ann. Glaciol.*, 23, 160–66.
916
917 Vericat, D., M. W. Smith, and J. Brasington (2014), Patterns of topographic change in sub-humid
918 badlands determined by high resolution multi-temporal topographic surveys, *Catena*, 120, 164–176.
919
920 Wallén, C. C. (1948), Glacial–meteorological investigations on the Karsa Glacier in Swedish
921 Lappland, *Geogr. Ann.*, 30(3–4), 451–672.
922

923 Wallén, C. C. (1949), Shrinkage of the Karsa Glacier and its probable meteorological causes,
924 *Geogr. Ann.*, 31(1–2), 275–291.
925
926 Wallén, C. C. (1959), The Karsa Glacier and its relation to the climate of the Torne Trask region,
927 *Geogr. Ann.*, 41(4), 236–244.
928
929 Wieringa, J. (1993), Representative roughness parameters for homogeneous terrain, *Bound.-Lay.*
930 *Meteorol.*, 63, 323–363.
931
932 **Tables**

933 **Table 1.** Summary of z_0 calculations.

934

Quantity	Profile-based	DEM-based	Cloud-based
Drag coefficient	0.5		
Effective obstacle height h^*(m)	2 × detrended standard deviation of profile perpendicular to wind	Mean height of all points above the detrended plane	
Ground area S (m^2)	For each 'roughness element' separately: $(X/f)^2$.	Full plot planar area	Full plot 3d surface area approximated by number of points after octree subsampling. No units.
Silhouette area s (m^2)	Uniform roughness elements approximated. Frontal area of a 'typical' roughness element calculated using equation 2 (see Figure 2A).	Exposed frontal area for each cardinal direction calculated across whole DEM. Only includes areas above detrended plane.	Surface area facing each cardinal direction estimated by counting number of points with normal vector 45° either side of that direction. Only points above detrended plane where normal vector is <80° from horizontal. No units.

935

936 **Table 2.** Summary of z_0 values for all plots. The wind direction is given (i.e. wind blowing from
937 'up-glacier' or from the 'true left', etc.). Thus, 'glacier flow parallel' profile-based values are for
938 profiles orientated across the glacier surface (i.e. perpendicular to the wind direction). Robust

939 metrics provided owing to the non-normality of the dataset (see outliers on the right panel of Figure
940 2A).
941

Z_0 method	Direction (wind)	Median (mm)	IQR (mm)
Profile	Glacier flow parallel	1.216	1.044
	Glacier flow perpendicular	0.760	1.778
	Average	**1.019**	**1.340**
DEM	Up-glacier	0.741	0.953
	Down-glacier	1.026	1.015
	Glacier flow parallel average	0.883	1.392
	True-Left	0.772	0.980
	True-Right	0.843	0.938
	Glacier flow perpendicular average	0.757	0.877
	Average	**0.820**	**1.110**
Point cloud	Up-glacier	1.071	1.160
	Down-glacier	0.941	0.883
	Glacier flow parallel average	0.998	1.009
	True-Left	1.227	0.977
	True-Right	1.222	1.081
	Glacier flow perpendicular average	1.269	1.029
	Average	**1.067**	**0.947**

942
943
944 **Figures**

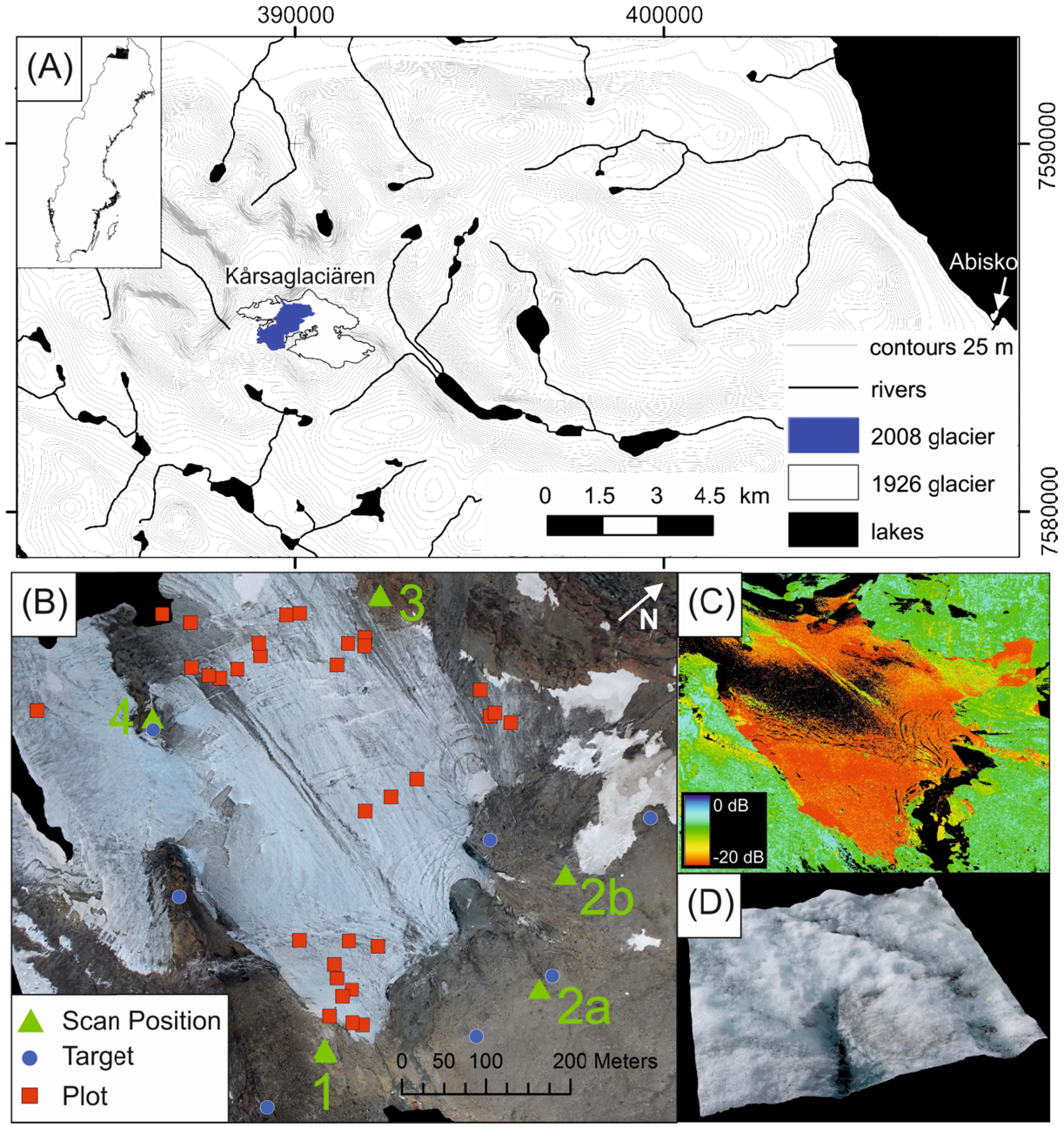

945

946

947 **Figure 1.** Study site. (A) Geographical location of Kårsaglaciären with 1926 and 2008 glacier

948 outlines; (B) Scan positions, targets and plot locations overlaid onto an orthophotograph of lower

949 Kårsaglaciären generated from glacier-scale SfM (not contemporaneous with plot surveys and used

950 to generate an orthophotograph only). Note the location of Scan 2 varied slightly between the two

951 surveys; (C) oblique viewpoint of TLS point cloud of the lower Kårsaglaciären rendered by return

952 reflectance (dB) displaying areas of wet ice oblique to the TLS that exhibited low point density (in

black); (D) example SfM-MVS plot dense point cloud viewed obliquely (Plot 1, supraglacial channels, approx. 2 x 2 m).

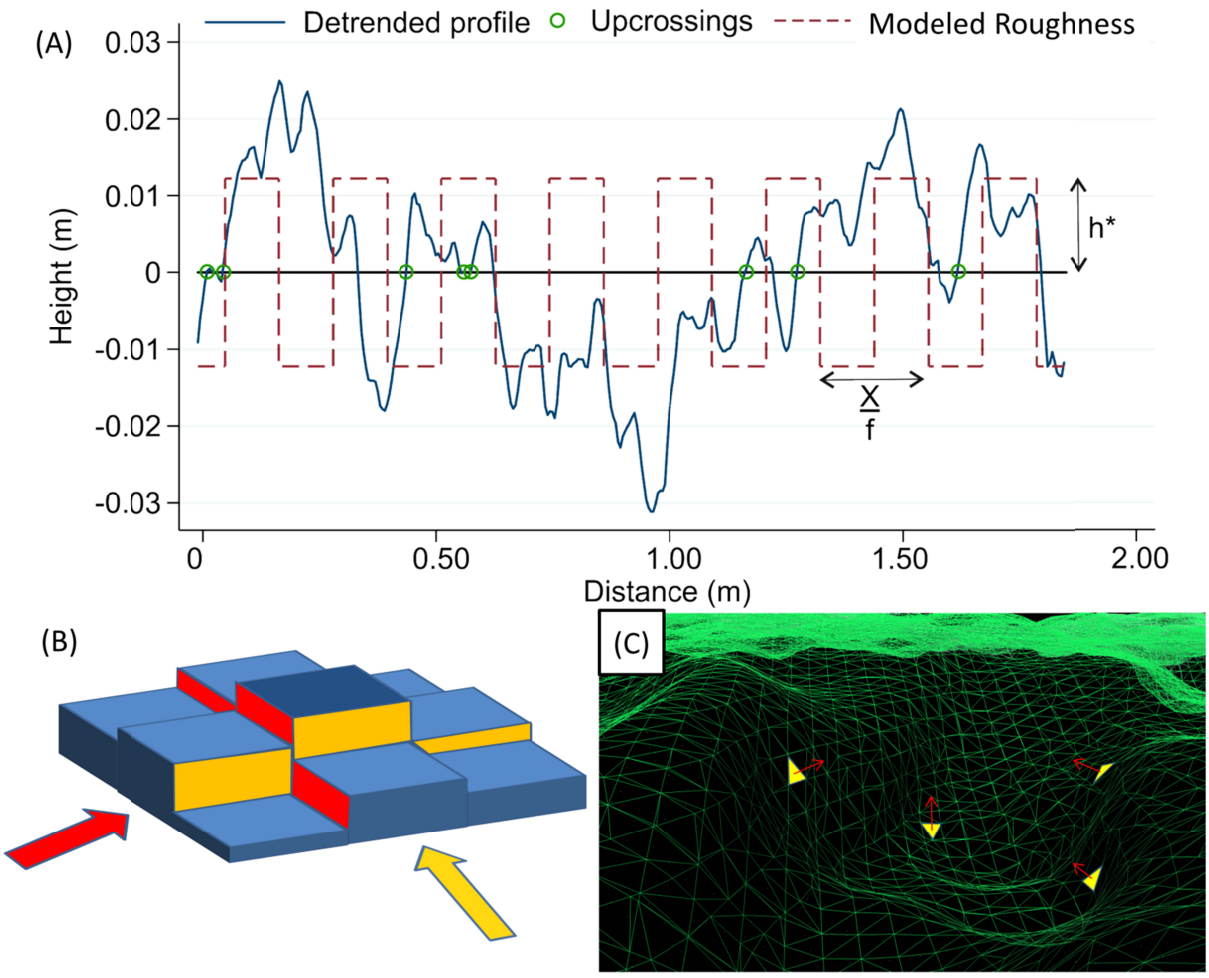

Figure 2. Schematic illustrations of z_0 calculations. (A) Conventional profile-based approach; (B) DEM-based approach highlighting frontal area for two orthogonal wind directions; (C) demonstration of normal vectors on a triangulated wireframe mesh of a point cloud (for illustration only).

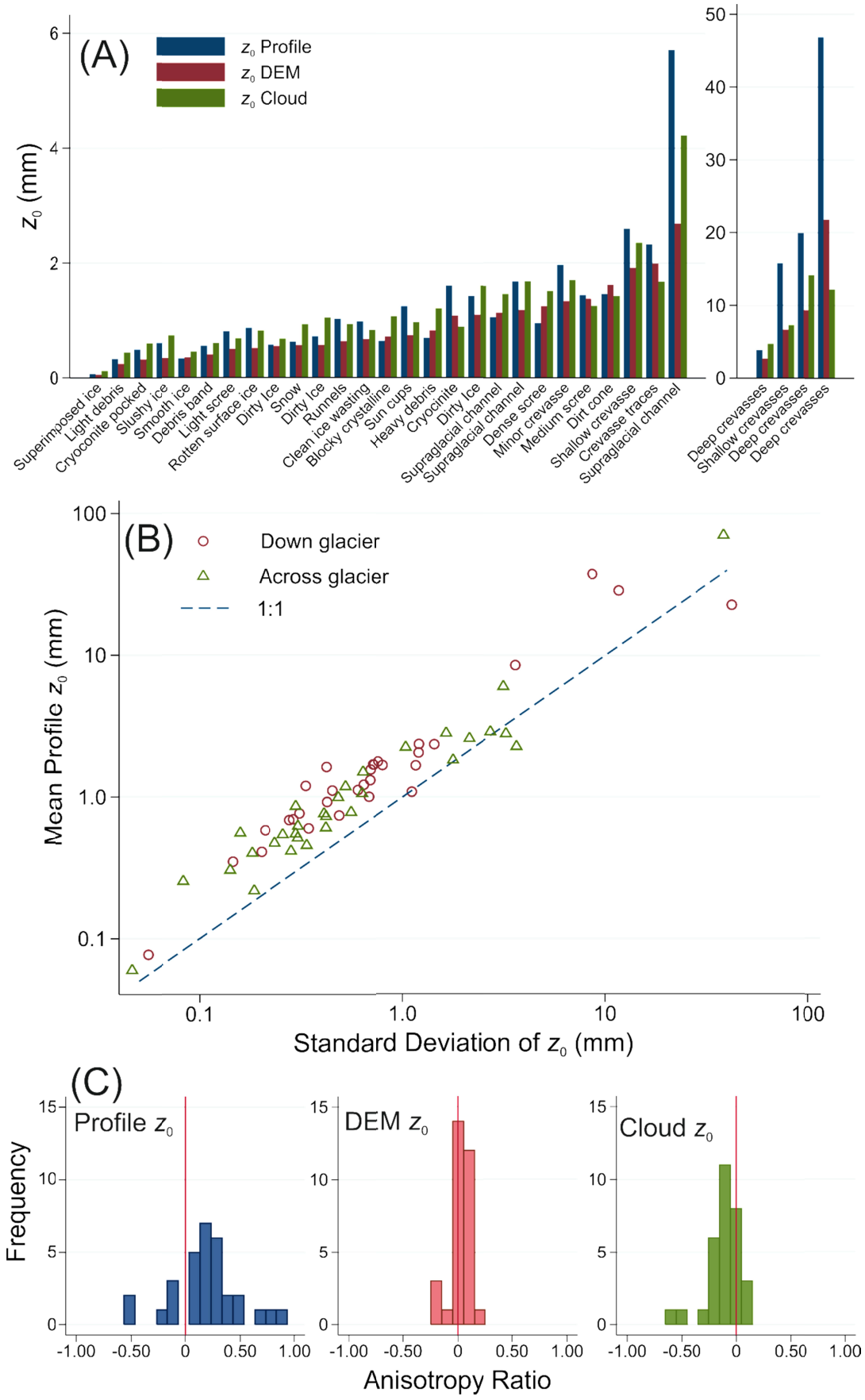
(A)
z_0 Profile
z_0 DEM
z_0 Cloud
z_0 (mm)
Superimposed ice
Light debris
Cryoconite pocked
Slushy ice
Smooth ice
Debris band
Light scree
Rotten surface ice
Dirty Ice
Snow
Dirty Ice
Runnels
Clean ice wasting
Blocky crystalline
Sun cups
Heavy debris
Cryocinite
Dirty Ice
Supraglacial channel
Supraglacial channel
Dense scree
Minor crevasse
Medium scree
Dirt cone
Shallow crevasse
Crevasse traces
Supraglacial channel
Deep crevasses
Shallow crevasses
Deep crevasses
Deep crevasses
(B)
Down glacier
Across glacier
1:1
Mean Profile z_0 (mm)
Standard Deviation of z_0 (mm)
(C)
Profile z_0
DEM z_0
Cloud z_0
Frequency
Anisotropy Ratio

962

963 **Figure 3.** (A) Variability of z_0 between plot surfaces (ordered by z_0 DEM). See Table S3 for values.
964 Mean profile-based z_0 values presented for each plot. (B) Relationship between mean and standard
965 deviation of profile-based z_0 values presented separately for each orthogonal direction. Note log-log
966 scale. (C) Summary of anisotropy ratio values for each method of z_0 calculation.
967

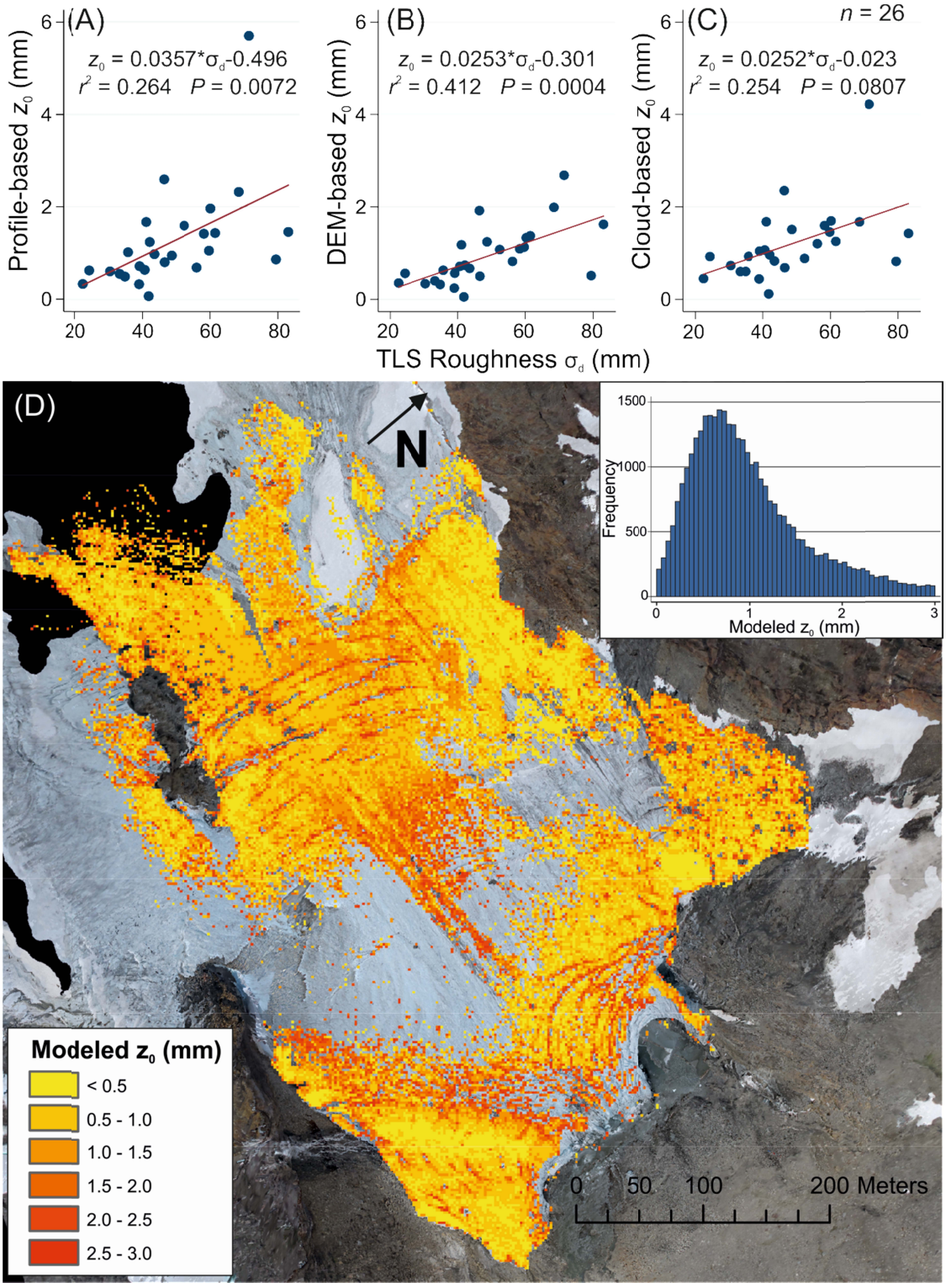

968

969 **Figure 4** (A-C) Relationships between directionally averaged z_0 values and sub-grid TLS roughness

970 (represented by the detrended standard deviation of elevations). Model fits correspond to the

971 regression parameters indicated. (D) Map of modeled glacier z_0 using TLS-derived sub-grid

972 roughness to upscale DEM-based z_0 (2 m resolution). Gaps relate to areas with insufficient TLS

973 data to compute sub-grid roughness or areas where predicted z_0 is > 3 mm and beyond the range of
974 the relationship demonstrated in Figure 4B. The distribution of modeled z_0 values is shown (inset).
975

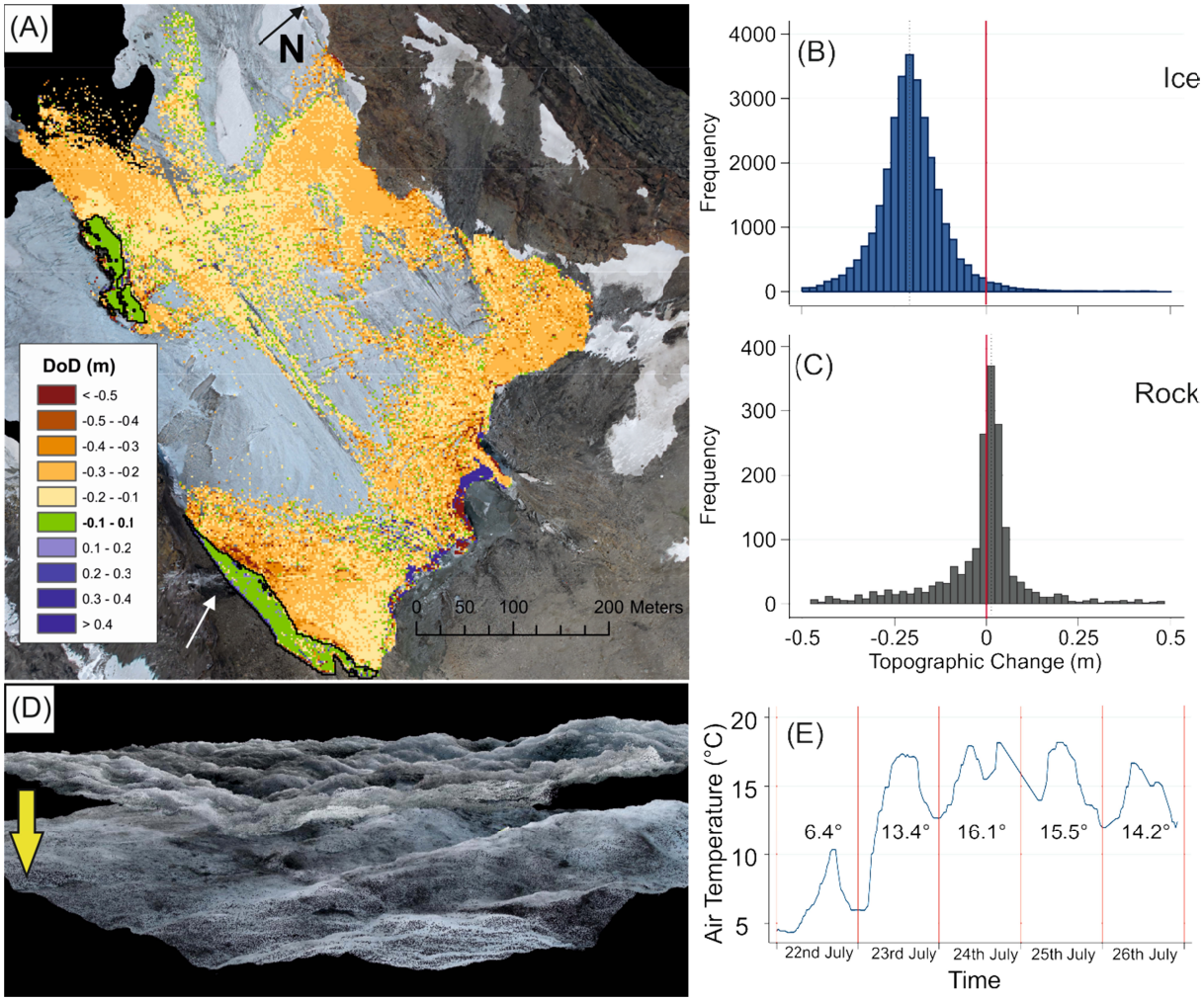

976
977

978 **Figure 5.** (A) DEM of Difference from repeat TLS over a three day interval. Bedrock areas are
979 outlined in black. The waterfall supplying a subglacial stream is indicated with a white arrow. (B)
980 Frequency histogram of observed topographic changes for ice surfaces and (C) for rock and
981 proglacial debris surfaces. Only changes ±0.5 m shown for clarity. (D) Example of lowering
982 observed from repeat SfM-MVS dense point clouds (Dirt Ice plot over a 3 day interval showing an
983 average surface elevation change of 0.23 m); (E) 30-minute smoothed temperature data recorded at

the AWS over the survey interval. Mean daily temperatures reported for each day. A data gap spanning 24th and 25th July has been interpolated.

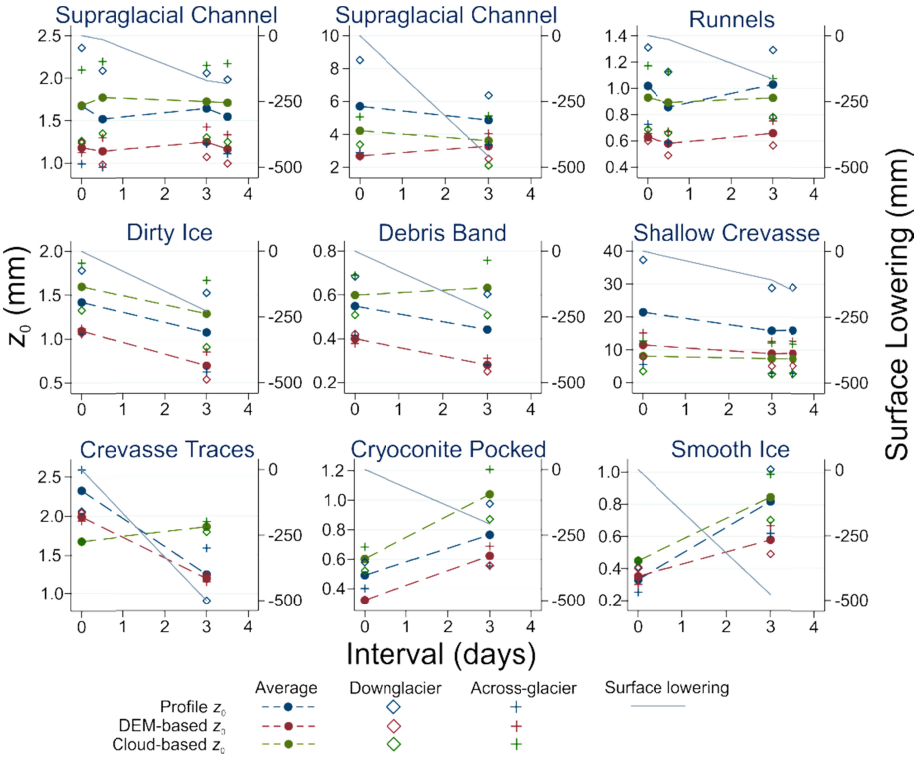

Figure 6. Plot-scale changes in z_0 values with surface lowering over several days of intense melting (Figure 5E). Note different scales on z_0 axes for improved clarity of changes within each plot. Survey intervals were not exactly contemporaneous with the DoD in Figure 5A.

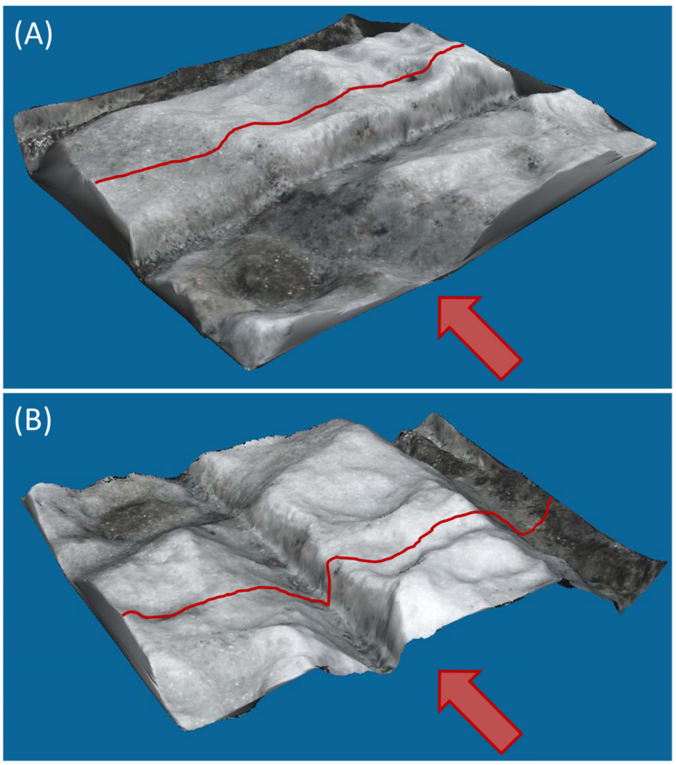

Figure 7. Demonstration of differences between z_0 anisotropy ratios for different calculation methods. The plot surface in (A) is rotated through 90 degrees in (B), while the prevailing wind direction remains constant. A greater frontal area is exposed to the prevailing wind in (A); however a profile perpendicular to the wind direction shows greater topographic variability in (B).